

Numerical Analysis of Ground Testing for the Intake Device of an Atmosphere-Breathing Electric Propulsion

IEPC-2025-288

*Presented at the 39th International Electric Propulsion Conference, Imperial College London, London, United Kingdom
14-19 September 2025*

Geonwoong Moon¹ and Eunji Jun²

Korea Advanced Institute of Science and Technology, Daejeon, 34141, Republic of Korea

Minwoo Yi³, Hyunjin Choi⁴, and Kangmin Park⁵

Agency for Defense Development, Daejeon, 34186, Republic of Korea

Younho Kim⁶, Jaecheong Lee⁷, Jeongjae Lee⁸

Gahee Joo⁹, Seungho Shin¹⁰, Se Lee¹¹, and Yunhwang Jeong¹²

Satrec Initiative, Daejeon, 34054, Republic of Korea

Atmosphere-breathing electric propulsion (ABEP) is a promising technology for long-term orbit maintenance in very-low-Earth orbit. The intake device plays a crucial role in capturing and supplying propellant, and its capture efficiency is a key indicator of drag-compensation feasibility. For experimental evaluation, an EP plasma plume can be used as a particle-flow generator to simulate the VLEO atmosphere in ground facilities. This study numerically investigates the interaction of an EP plasma plume with an intake device to establish guidelines for measuring capture efficiency in conventional vacuum facilities. A hybrid PIC-DSMC method with ion-surface interaction models is employed to simulate the plasma plume incident on the intake. The composition of the captured flow is governed by beam ion energy and species mass: lowering the energy and using lighter atmospheric constituents increase plume divergence and promote neutralization, yielding a neutral-dominated outlet flow. Sputtering of the intake surface becomes non-negligible at high energies but can be mitigated by operating at appropriately low beam energies. The results demonstrate that simultaneous ion and neutral diagnostics are required for reliable capture-efficiency evaluation when using EP plasma plumes in ground facilities.

¹Ph.D. Student, Department of Aerospace Engineering, kw4046@kaist.ac.kr

²Associate Professor, Department of Aerospace Engineering, eunji.jun@kaist.ac.kr

³Research Engineer, Satellite Systems PMO, minwooyi@add.re.kr

⁴Research Engineer, Satellite Systems PMO, hchoi1add@add.re.kr

⁵Research Engineer, Satellite Systems PMO, kmp2002@add.re.kr

⁶Research Engineer, Space Technology Research Center, yhk@satreci.com

⁷Research Engineer, Space Technology Research Center, jclee@satreci.com

⁸Research Engineer, Space Technology Research Center, jjlee@satreci.com

⁹Research Engineer, Space Technology Research Center, ghjoo@satreci.com

¹⁰Research Engineer, Space Technology Research Center, sh_shin@satreci.com

¹¹Research Engineer, Space Technology Research Center, sallyselee@snu.ac.kr

¹²Research Engineer, Space Technology Research Center, yhjung@satreci.com



Nomenclature

| | | |
|-----------|-------------------------|---|
| Kn | Knudsen number | Subscripts |
| λ | mean free path | ∞ freestream condition |
| L | characteristic length | in inlet condition |
| s | speed ratio | out outlet condition |
| v | velocity | c collision pair |
| T | temperature | r relative properties |
| k_B | Boltzmann constant | mex momentum-exchange |
| m_p | particle mass | cex charge-exchange |
| \dot{N} | particle flow rate | e electron properties |
| n | number density | i ion properties |
| η_c | capture efficiency | n neutral atom properties |
| CR | compression ratio | ref reference properties |
| f | distribution function | \parallel parallel component to the surface |
| \vec{F} | external force | \perp normal component to the surface |
| σ | collision cross-section | |
| Ω | solid angle | Superscripts |
| ϕ | plasma potential | $*$ post-collisional properties |
| e | elementary charge | |
| γ | specific heat ratio | |
| p | momentum | |

I. Introduction

Atmosphere-breathing electric propulsion (ABEP) is an emerging space propulsion system for efficient orbit maintenance in very-low-Earth-orbit (VLEO) below 450 km, where enhanced optical resolution and reduced launch cost are obtainable¹. Similar to air-breathing engines for aircraft, the ABEP system captures and compresses atmospheric flow in the ram direction using an intake device². The captured atmospheric gas is then transferred to the ABEP thruster as a propellant. The atmospheric propellant is ionized and accelerated inside the thruster by electromagnetic force, generating thrust for drag compensation maneuvers. Through *in situ* acquisition of propellant, ABEP can facilitate long-term missions in VLEO without depleting onboard propellant^{3,4}. ABEP is considered to be competitive with conventional electric propulsion (EP) in an altitude range of 160–250 km⁵.

The ABEP captures the rarefied VLEO atmosphere, and its degree of rarefaction can be represented with the Knudsen number Kn :

$$Kn = \lambda/L, \quad (1)$$

which is a ratio between the mean free path λ and characteristic length L . The flow regime in VLEO atmosphere is characterized as free molecular flow (FMF), having Kn greater than 10 above 160 km altitude². VLEO satellites have orbital velocities exceeding 7 km/s, which is more than five times faster than the thermal velocity of atmospheric particles. The speed ratio s is defined as the ratio of the freestream velocity v_∞ to the most probable thermal velocity v_{mp} :

$$s = \frac{v_\infty}{v_{mp}} = \frac{v_\infty}{\sqrt{\frac{2k_B T_\infty}{m_p}}}. \quad (2)$$

The flow is categorized as a thermal flow for a speed ratio $s < 5$, where Brownian motion appears significantly in the particle kinetics. On the other hand, the flow becomes hyperthermal when $s > 5$. The collective motion is predominant, rather than the random motion of the particles in the hyperthermal flow. The freestream to the ABEP intake device is a hyperthermal flow wherein the velocity of the individual gas particles is highly collimated in the ram direction. Intermolecular collision and gas-surface interaction can scatter the particles, reducing the speed ratio s . The hyperthermal freestream turns into a thermal flow as the bulk



motion diminishes and the random motion intensifies. This process is called thermalization and provides a compression effect for the intake device of ABEP by stagnating the freestream particles².

Developing an efficient intake device is crucial for realizing a feasible ABEP system for complete drag compensation maneuver^{6,7}. The capturing process of hyperthermal and rarefied gas flows has been extensively investigated in previous studies using numerical methods, resulting in the development of various optimal intake device designs aimed at achieving high performance^{2,6,8-23}. The intake performance can be measured with compression ratio CR and capture efficiency η_c ,

$$CR = \frac{n_{out}}{n_\infty}. \quad (3)$$

$$\eta_c = \frac{\dot{N}_{out}}{\dot{N}_{in}} = \frac{n_{out} u_{out} A_{out}}{n_\infty u_\infty A_{in}}, \quad (4)$$

The compression ratio CR represents the ratio of the number density of the captured propellant to that of the freestream atmosphere. The capture efficiency η_c represents the flow rate ratio of the captured gas entering the thruster to the total atmospheric freestream incident on the intake device's inlet area. η_c is a critical parameter for assessing drag-compensation feasibility, as it quantifies the capability of supplying propellant to the ABEP thruster.

Beyond numerical characterization, ground tests have been conducted to validate both the functionality of intake devices and the feasibility of the ABEP concept²⁴. Electric propulsion (EP) systems can be employed as particle flow generators (PFGs) to simulate rarefied, hyperthermal flow with a consistent incident flux to intake devices²⁴⁻²⁷. Unlike the predominantly neutral VLEO atmosphere, the charged particles in EP plasma plumes can interact with the surface of intake devices through mechanisms such as electric acceleration, sheath formation, and neutralization²⁸. Moreover, direct impingement of high-speed ions might induce sputtering²⁹. Accounting for these altered surface interactions is essential when evaluating intake performance in ground tests employing EP plasma plumes.

The ground tests can be classified into end-to-end testing and stand-alone intake device testing. End-to-end testing employs an integrated intake device–thruster assembly, and several campaigns have demonstrated ABEP operation by generating thrust from the captured gas flow^{25,26,30}. However, characterizing intake performance remains challenging in end-to-end testing, as the flow properties at the outlet of the intake device cannot be measured separately. Recently, stand-alone intake device testing apparatus have been proposed to investigate intake performance^{31,32}. These apparatus enable direct measurement of the captured flow rate for evaluating η_c , but require specialized facilities with segmented auxiliary reservoirs and pumps in addition to conventional vacuum chambers. If intake performance could be measured in conventional vacuum chambers, stand-alone intake device testing would be more accessible using existing diagnostics; however, prior understanding of the captured flow is required to select appropriate techniques.

This study numerically investigates the EP plasma plume flow into an intake device to establish guidelines for evaluating η_c in conventional vacuum chambers. The exhaust plasma plume of a gridded ion thruster is simulated under facility background pressure and directed into the intake device to assess outlet flow characteristics. The analysis considers variations in beam ion energy and species mass. A hybrid Particle-in-Cell/Direct Simulation Monte Carlo (PIC-DSMC) method is employed, incorporating a polytropic electron fluid model and physical models for intermolecular collisions, gas-surface interaction, and ion-surface interactions.

II. Physical Models and Numerical Methodology

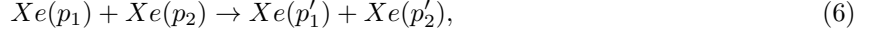
The rarefied gas flow and collisional plasma plume flow can be described by the Boltzmann equation (BE):

$$\frac{\partial}{\partial t}(nf) + \vec{v} \cdot \frac{\partial}{\partial \vec{r}}(nf) + \frac{\vec{F}}{m_p} \cdot \frac{\partial}{\partial \vec{v}}(nf) = \int_{-\infty}^{\infty} \int_0^{4\pi} n^2 [f^* f_c^* - f f_c] v_r \sigma d\Omega d\vec{v}_1, \quad (5)$$

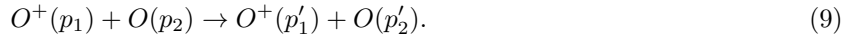
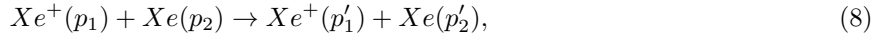
where the BE governs the time evolution of the particle distribution function f in phase space, spanned by position \vec{r} and velocity \vec{v} . The right-hand side represents the binary collision operator, while the left-hand side accounts for particle advection under the influence of external forces \vec{F} , including the self-consistent electric field arising from the collective motion of charged particles.



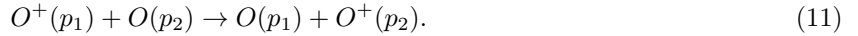
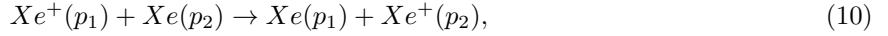
Momentum exchange (MEX) collisions between neutral atoms are modeled using the variable hard sphere (VHS) model, which assumes isotropic scattering with a total cross section (TCS) dependent on the relative velocity v_r of the colliding pair³³. Following MEX collisions are simulated with VHS model:



In contrast, ion–atom collisions are characterized as long-range charge–induced dipole interactions, where small-angle scattering dominates. Accurate simulation of ion–atom interactions requires not only TCS but also detailed modeling of the differential cross section (DCS). This study employs the generalized collision cross-section Model (GCCM) developed for monatomic ion–atom interactions³⁴. GCCM evaluates both TCS and DCS as functions of atomic number and collision energy, enabling the accurate determination of deflection angles and post-collisional momenta for ions and atoms, respectively. Following ion-atom MEX collisions are modeled with GCCM:



In addition to the MEX process, ion–atom collisions can involve charge exchange (CEX):



For the resonant CEX of Eqs. (10) and (11), the TCS of CEX is assumed to be equivalent to that of the MEX estimated by GCCM^{35–40}.

Gas-surface interaction (GSI) of neutral atoms is modeled using the Maxwell model, which describes the kinetic energy of reflected particles through the energy accommodation coefficient α_ϵ :

$$\alpha_\epsilon = \frac{T_{k,pre} - T_{k,post}}{T_{k,pre} - T_s}, \quad (12)$$

where $T_{k,pre}$ and $T_{k,post}$ represent the kinetic energy of a particle before and after the GSI, respectively, while T_s denotes the surface temperature where the particle accommodates. A specular reflection occurs when $\alpha_\epsilon = 0$, whereas a fully diffuse reflection takes place when $\alpha_\epsilon = 1$. On the other hand, ion–surface interaction (ISI) is modeled for scattering with sheath acceleration, neutralization, and sputtering. In the vicinity of a surface, a plasma sheath develops due to the mobility difference between ions and electrons²⁸. The sheath potential ϕ_{sh} between plasma and a floating surface can be derived from the impinging ion and electron current balance:

$$J_e = J_{i,\perp}. \quad (13)$$

Here, the ion current density normal to the surface is denoted by $J_{i,\perp}$, while the electron current density is represented by J_e . Considering the half-Maxwellian flux of electrons at T_e , the sheath potential ϕ_{sh} can be expressed as a function of $J_{i,\perp}$:

$$\phi_{sh} = \frac{k_B T_e}{e} \left[\ln \left(\frac{4J_{i,\perp}}{en_e} \right) - \frac{1}{2} \ln \left(\frac{8k_B T_e}{\pi m_e} \right) \right]. \quad (14)$$

Using the calculated ϕ_{sh} , the terminal ion velocity components $v'_{i,\perp}$ and $v'_{i,\parallel}$ incident on the floating surface are corrected as:

$$v'_{i,\parallel} = v_{i,\parallel}, \quad (15)$$

$$v'_{i,\perp} = \sqrt{v_{i,\perp}^2 + \frac{2e\phi_{sh}}{m_i}}. \quad (16)$$

After passing through the sheath, ions impinging on the surface may undergo scattering, neutralization, or sputtering. Scattering is modeled using the Maxwell model, while neutralization is applied with a probability P_{neut} , producing reflected neutral atoms. Sputtering of surface atoms depends on the incident ion energy E



and grazing angle θ . The total sputtering yield $Y(E, \theta)$ is expressed as the product of the energy-dependent yield $Y(E, 0)$ and the angular-dependent yield $Y'(\theta)$:

$$Y(E, \theta) = Y(E, 0) \cdot Y'(\theta). \quad (17)$$

Semi-empirical formulae suggested in Yim's paper are employed to compute the sputtering yield, which are Eckstein's energy dependence model and reformulated Wei's angular dependence model^{41–43}:

$$Y(E, 0) = Q s_n \frac{\left(\frac{E}{E_{th}} - 1\right)^\mu}{\frac{\lambda}{w} + \left(\frac{E}{E_{th}} - 1\right)^\mu}, \quad (18)$$

$$Y'(\theta) = \frac{1}{1 + (\beta/\alpha)^2 \tan^2 \theta} \exp\left(\frac{1}{2} \left(\frac{a}{\alpha}\right)^2 \left[1 - \frac{1}{1 + (\beta/\alpha)^2 \tan^2 \theta}\right]\right). \quad (19)$$

Here, $(Q, \lambda, \mu, E_{th})$ and $(\beta/\alpha, a/\alpha)$ are fitting parameter sets for the respective models. The reduced nuclear stopping power s_n is formulated from the Krypton–Carbon (KC) potential, and w is a parameter dependent on reduced energy⁴¹. The number of sputtered atoms is determined from $Y(E, \theta)$, and their energies E_{spt} are sampled according to the Sigmund–Thompson distribution⁴⁴:

$$f(E_{spt}) \propto \frac{E_{spt}}{(E_{spt} + U_B)^{3-2l}}, \quad (20)$$

where U_B is the surface binding energy and l is the interatomic potential exponent²⁹. The angular distribution of sputtered atoms leaving the surface is assumed to follow a cosine law²⁹.

A hybrid kinetic simulation method is employed to obtain a stochastic solution of the Boltzmann equation (BE) with the physical models, combining two complementary approaches: Particle-in-Cell (PIC) and Direct Simulation Monte Carlo (DSMC). The hybrid PIC–DSMC method treats ions and atoms as discrete particles, whereas electrons are modeled as a fluid. The PIC and DSMC methods work in tandem to compute electrostatic accelerations and collisions that govern particle motion over time. The DSMC method provides the primary framework through particle sorting, advection, and collision procedures, while the PIC method supplies the electrostatic acceleration of charged particles via charge density assignment, field updating, and field interpolation³⁴. The PIC method calculates the plasma potential from the spatial charge density and a polytropic cooling model of the electron fluid, whereby the electron momentum equation is reduced to^{34,35,45–47}:

$$\phi = \begin{cases} \phi_{ref} + \frac{k_B T_{e,ref}}{e} \ln\left(\frac{n_e}{n_{e,ref}}\right) & \text{for } \gamma = 1, \\ \phi_{ref} + \frac{k_B T_{e,ref}}{e} \frac{\gamma}{\gamma - 1} \left[\left(\frac{n_e}{n_{e,ref}}\right)^{\gamma-1} - 1\right] & \text{for } \gamma > 1. \end{cases} \quad (21)$$

This study adopts a specific heat ratio of $\gamma = 1.3$ for the plasma plume flow, and charge quasi-neutrality is assumed as $n_e \approx n_i$ ^{34,48}. The electric field is obtained by finite differencing of the potential and interpolated to individual particles to assign the corresponding electrostatic acceleration. The hybrid PIC–DSMC code employed in this study is adopted from Moon *et al.*, developed on the basis of the SPARTA DSMC framework^{34,49}.

III. Simulation Settings

The plasma plume of a gridded ion thruster is simulated in an axisymmetric domain with 60 cm in length and 20 cm in radius, as shown in Fig. 1. The thruster exit plane has a diameter of 10 cm. Ions are exhausted from the exit plane with a divergence angle of 15°, and the ion number density profile is prescribed as a bivariate Gaussian distribution with respect to the radial position. Multiply charged ions are neglected. Neutral atoms are emitted with a half-Maxwellian velocity distribution at $T_n = 500$ K. Four simulation cases are defined according to the exhaust conditions, varying ion energy and propellant species. The Xe 1000 eV case represents the conventional operating condition of ion thrusters with xenon propellant. The Xe 250 eV case corresponds to a halved ion velocity v_i , while the Xe 40 eV case yields v_i consistent with the VLEO freestream velocity. To investigate the effect of propellant substitution with a lighter atmospheric



constituent, the O 5 eV case is defined using atomic oxygen propellant, with v_i also consistent with the VLEO freestream velocity. The cases and exhaust conditions are summarized in Table 1. All cases are configured with a constant flow rate of 3.3 sccm and an ionization degree of 90%. A facility background pressure of 5×10^{-6} torr is imposed in the simulations, with neutral particles at 300 K injected through the domain boundaries. At 30 cm downstream from the thruster exit plane, a parabolic intake device is placed,

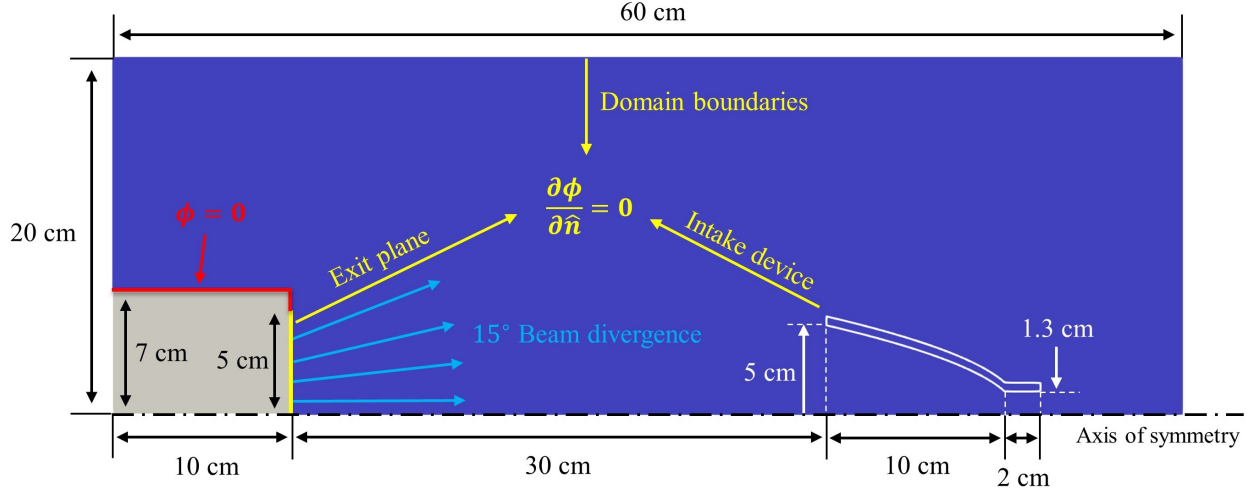


Figure 1: Simulation domain

Table 1: Exhaust conditions of ion thruster

| Properties | Xe 1000 eV | Xe 250 eV | Xe 40 eV | O 5 eV |
|--------------------|-----------------------|-----------------------|-----------------------|-----------------------|
| Species | | Xe/Xe^+ | | O/O^+ |
| n_n [m $^{-3}$] | | 1.00×10^{17} | | 3.48×10^{16} |
| v_n [m/s] | | 284 | | 815 |
| T_n [K] | | 500 | | |
| n_i [m $^{-3}$] | 4.55×10^{15} | 9.10×10^{15} | 2.28×10^{16} | 2.28×10^{16} |
| v_i [m/s] | 3.9×10^4 | 1.95×10^4 | 7.8×10^3 | 7.8×10^3 |
| T_i [eV] | | | 1 | |

with an inlet radius of 5 cm, an outlet radius of 1.3 cm, and a total length of 12 cm. The intake device is assumed to be composed of pyrolytic graphite, applying GSI and ISI properties specified in Table 2. For the O 5 eV case, the ion energy is lower than the surface binding energy; therefore, sputtering is neglected for O^+ ion impingement. The GSI and neutralization of ISI are also considered to the thruster's surface.

The computational domain is discretized using an adaptively refined five-level hierarchical structured grid. For the PIC calculations, the thruster exit plane and the intake device are treated with Neumann boundary conditions, imposing a zero potential gradient, while the remaining thruster surfaces are grounded. The timestep is set to 5×10^{-8} s to resolve ion plasma oscillation periods throughout the domain. Disparate weighting factors of 1.0 and 0.01 are applied to neutral atoms and ions, respectively. In addition, radial cell weighting is employed to ensure an even distribution of simulation particles within the axisymmetric domain. Each case is iterated up to 800,000 steps, sampling macroscopic flow properties after the flow reaches steady state.

IV. Results

Fig. 2 shows contour diagrams of the ion number density distribution. The ion beam expands downstream and enters the intake device. In Figs. 2(a)–(c), the plume envelope exhibits greater divergence as the exhaust

Table 2: GSI and ISI properties

| Interaction | Parameter | Value | ref. |
|-------------|-------------------|--------|------|
| GSI | α_ϵ | 1.0 | * |
| | T_s | 500 K | * |
| ISI | P_{neut} | 1.0 | * |
| | Q | 4.0 | 41 |
| | λ | 0.8 | 41 |
| | μ | 1.8 | 41 |
| | E_{th} | 21 | 41 |
| | β/α | 0.88 | 41 |
| | a/α | 2.20 | 41 |
| | U_B | 7.4 eV | 29 |
| | l | 1/3 | 29 |

* assumed properties

ion energy decreases, since diffusive transport and transverse electric acceleration become more significant due to the higher charge density in the thruster near-field. Owing to the lighter mass of O ions compared with Xe ions, the O 5 eV case in Fig. 2(d) produces a more diffusive plume than the Xe 40 eV case in Fig. 2(c), even though both cases share the same exhaust ion number density and velocity. This implies that reducing ion acceleration and substituting the propellant with atmospheric constituents can improve similarity to VLEO freestream composition; however, the resulting higher divergence may hinder the simulation of hyperthermal flows characterized by highly aligned particle trajectories.

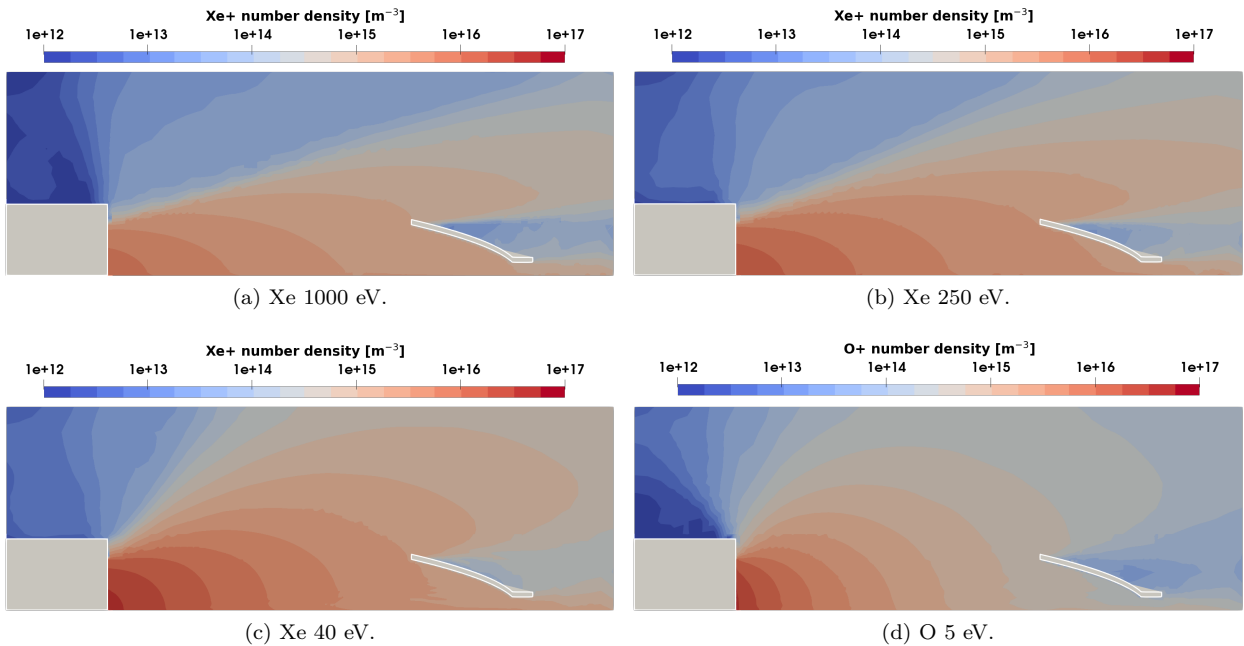


Figure 2: Ion number density distribution.

As ions impinge on the internal surface of the intake device, they undergo neutralization and form compressed gas inside, as shown in the neutral atom density distribution in Fig. 3. Since higher exhaust ion energy produces a more collimated beam, a larger ion flux enters the intake device, resulting in a higher concentration of neutral atoms. For the Xe 1000 eV case, the inlet ion flux is $3.96 \times 10^{19} \text{ m}^{-2}\text{s}^{-1}$. This

decreases to $3.37 \times 10^{19} \text{ m}^{-2}\text{s}^{-1}$ and $1.65 \times 10^{19} \text{ m}^{-2}\text{s}^{-1}$ for the Xe 250 eV and Xe 40 eV cases, respectively. The O 5 eV case exhibits the lowest inlet ion flux of $7.56 \times 10^{18} \text{ m}^{-2}\text{s}^{-1}$, which is 5.2 times lower than that of the Xe 1000 eV case. Accordingly, the neutral atom concentration inside the intake device is highest for the Xe 1000 eV case and lowest for the O 5 eV case, where the density increase remains less than 10% compared to the background pressure. Since a large fraction of ions neutralize within the intake device, the neutral atom flux escaping the outlet increases to 4.9–13.4 times the incoming neutral flux at the inlet. In contrast, the ion flux at the outlet decreases to 48.3–62.4% of the inlet value. The ion and neutral fluxes at the inlet and outlet of the intake device are summarized in Table 3.

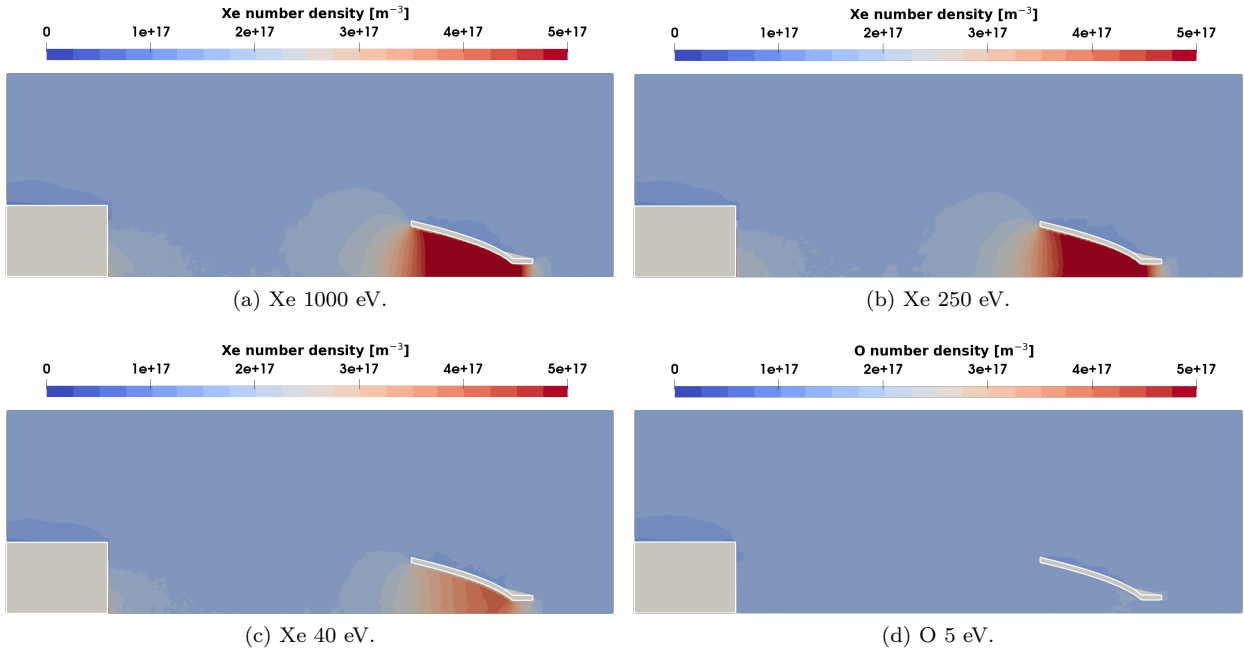


Figure 3: Neutral atom number density distribution.

Ion impingement on the intake device surface produces not only neutralized atoms but also sputtered atoms, depending on the incident energy. Fig. 4 shows the number density distribution of sputtered carbon atoms. For xenon projectiles in the 40–1000 eV energy range, the sputtering yield of pyrolytic graphite increases with ion energy⁴¹. Accordingly, the Xe 1000 eV case in Fig. 4(a) exhibits the most significant sputtering of C atoms, whereas the Xe 40 eV case shows a C number density less than 0.5% of that in the former case. The sputtered C atoms also pass through the outlet of the intake device, with fluxes of 2.24×10^{18} , 5.12×10^{17} , and $8.14 \times 10^{15} \text{ m}^{-2}\text{s}^{-1}$ for each case, as summarized in Table 3. The outlet flux of sputtered atoms may distort measurements of the captured flow rate through the intake device, thereby affecting the evaluation of capture efficiency η_c .

Fig. 5 shows the total outlet flux, combining ions, neutrals, and sputtered atoms. In the Xe 1000 eV case, the total flux is $5.28 \times 10^{19} \text{ m}^{-2}\text{s}^{-1}$, consisting of 46.7% ion flow, 49.0% neutral flow, and 4.2% sputtered flow. When the ion energy is reduced to 250 eV and 40 eV, the sputtered fraction decreases to 1.2% and 0.04%, respectively. This indicates that lowering the beam ion energy below 100 eV may be necessary to suppress sputtering on the intake device surface, thereby minimizing its influence on η_c evaluation. As the beam ion energy decreases, the ion fraction within the total outlet flux also decreases, as shown in Fig. 6. Moreover, the O 5 eV case exhibits an even lower ion fraction than the Xe 40 eV case. At low ion energy and mass, enhanced beam divergence reduces the probability of ions transmitting directly through the intake device to the outlet without ISI. Even though more than 86% of the inlet flow initially consists of ions, a substantial fraction is neutralized, resulting in a neutral-dominated flow at the outlet. Accordingly, measurement of neutral particles is essential for accurately evaluating η_c , in addition to ion diagnostics. Table 3 summarizes the estimated η_c obtained using different measurement approaches. When both ion and neutral atom flow rates are considered, the η_c of the parabolic intake device employed in this study is expected to be 7.14–8.23%, depending on the thruster exhaust conditions. However, if only plasma diagnostics are applied, η_c

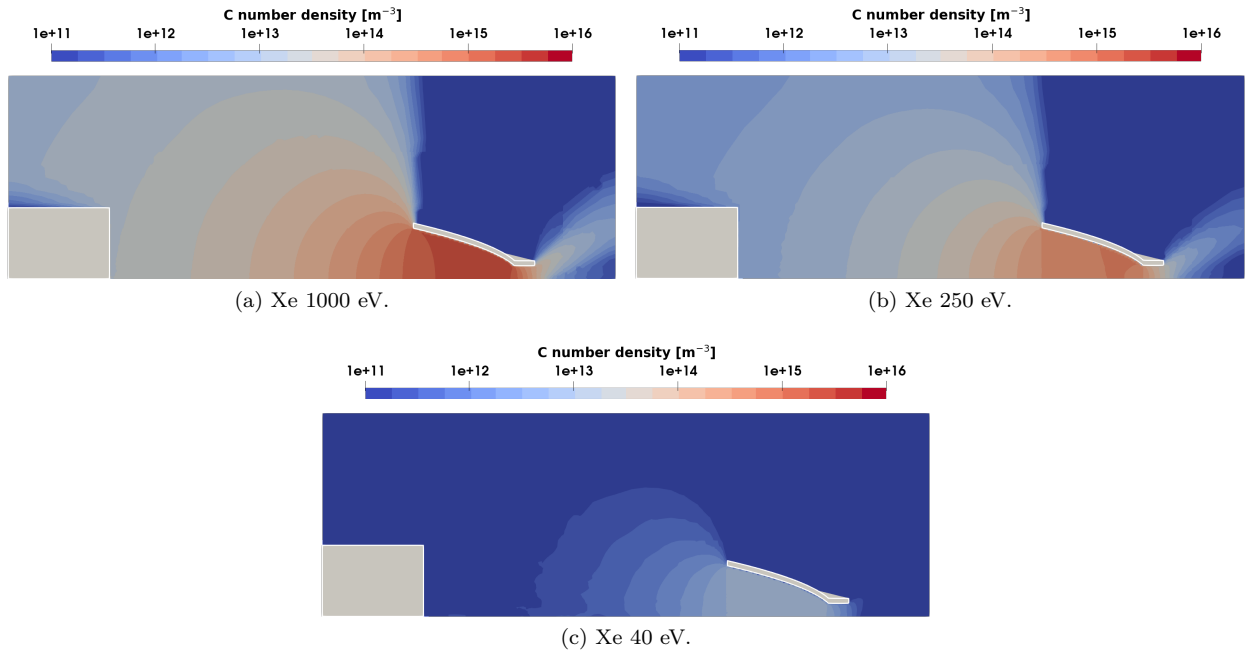


Figure 4: Sputtered C atom number density distribution.

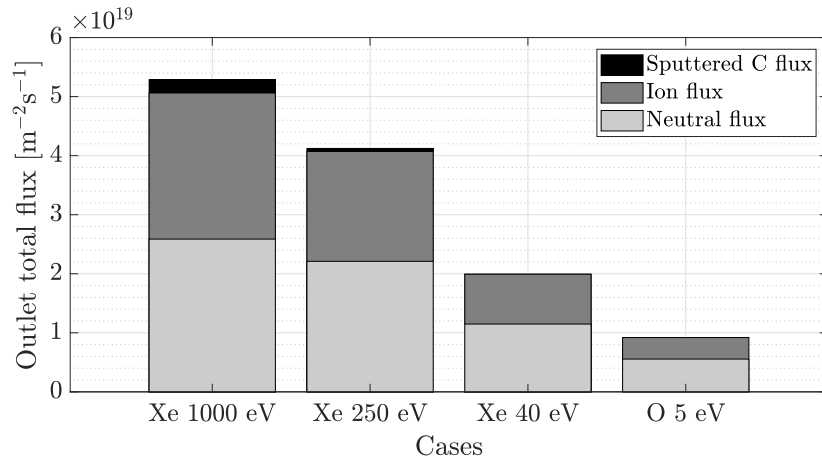


Figure 5: Outlet total flux and its composition

would be underestimated, yielding values in the range of 3.13–4.12%. Neutral-only measurement also would result biased η_c to 4.19–4.31%. These results indicate that simultaneous measurement of both ion and neutral flows is essential for reliable η_c evaluation in stand-alone intake-device testing using an EP plasma plume within conventional vacuum chambers.

V. Conclusion

This work numerically investigates how EP plasma plume–intake interactions govern measurable capture efficiency η_c in vacuum facilities. Plume ion energy and species mass influence plume divergence and ion neutralization, yielding neutral-dominated outlet flows. High energy of plume ions may increase wall sputtering that can bias the measurements. Reliable η_c evaluation requires simultaneous ion and neutral diagnostics and operation at plume ion energies below 100 eV to limit sputter-induced error. Under these

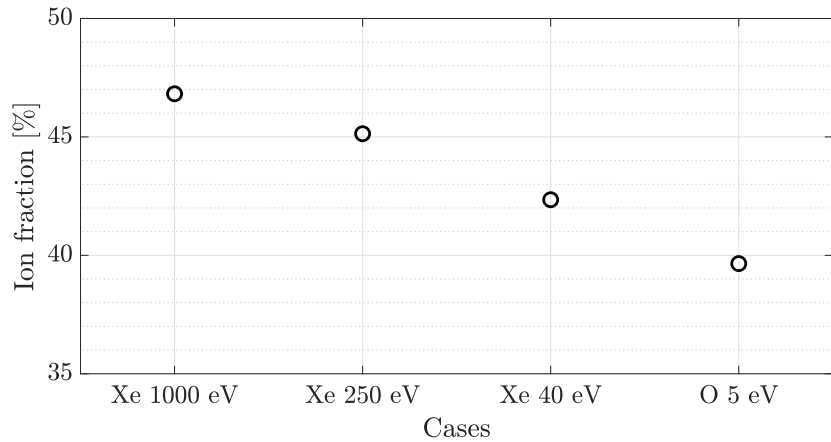


Figure 6: Ion fraction of the outlet flux

Table 3: Inlet/outlet flux and η_c for different cases

| Properties | Xe 1000 eV | Xe 250 eV | Xe 40 eV | O 5 eV |
|--|-----------------------|-----------------------|-----------------------|-----------------------|
| Inlet ion flux [$\text{m}^{-2} \text{s}^{-1}$] | 3.96×10^{19} | 3.37×10^{19} | 1.65×10^{19} | 7.56×10^{18} |
| Inlet neutral atom flux [$\text{m}^{-2} \text{s}^{-1}$] | 1.93×10^{18} | 1.97×10^{18} | 1.64×10^{18} | 1.14×10^{18} |
| Outlet ion flux [$\text{m}^{-2} \text{s}^{-1}$] | 2.47×10^{19} | 1.86×10^{19} | 8.44×10^{18} | 3.65×10^{18} |
| Outlet neutral atom flux [$\text{m}^{-2} \text{s}^{-1}$] | 2.59×10^{19} | 2.21×10^{19} | 1.15×10^{19} | 5.55×10^{18} |
| Outlet sputtered atom flux [$\text{m}^{-2} \text{s}^{-1}$] | 2.24×10^{18} | 5.12×10^{17} | 8.14×10^{15} | - |
| η_c (ion-only) [%] | 4.12 | 3.52 | 3.13 | 2.83 |
| η_c (neutral-only) [%] | 4.21 | 4.19 | 4.26 | 4.31 |
| η_c (Total) [%] | 8.23 | 7.71 | 7.39 | 7.14 |

conditions, stand-alone intake tests in conventional vacuum chambers may provide a practical basis for intake performance evaluation and ABEP feasibility analysis. Because η_c is sensitive to surface treatment and coating materials, future work will examine GSI/ISI variations in ground tests^{2,50-54}. Moreover, similarity between ground-test and on-orbit performance will be addressed to establish the validity of ground-based measurements.

Acknowledgments

This work was supported by the Agency For Defense Development by the Korean Government (UG233092TD). This work was supported by the National Supercomputing Center with supercomputing resources including technical support(KSC-2025-CRE-0427).

References

- ¹ Filatyev, A. S., Golikov, A. A., Erofeev, A. I., Khartov, S. A., Lovtsov, A. S., Padalitsa, D. I., Skvortsov, V. V., and Yanova, O. V., "Research and development of aerospace vehicles with air breathing electric propulsion: Yesterday, today, and tomorrow," *Progress in Aerospace Science*, Vol. 136, 2023, pp. 100877.
- ² Moon, G., Yi, M., Park, K., Kim, Y., Yoon, H., and Jun, E., "Performance characterization and kinetic analysis of atmosphere-breathing electric propulsion intake device," *Vacuum*, Vol. 212, 2023, pp. 112066.
- ³ Schonherr, T., Komurasaki, K., Romano, F., Massuti-Ballester, B., and Herdrich, G., "Analysis of

atmosphere-breathing electric propulsion," *IEEE Transactions on Plasma Science*, Vol. 43, No. 1, 2015, pp. 287–294.

- ⁴ Jun, E., "Exploring Atmosphere-Breathing Electric Propulsion: Insights and Challenges for Future VLEO Satellite Applications," *33rd International Symposium on Rarefied Gas Dynamics (Göttingen, Germany)*, 2024.
- ⁵ Ko, Y., Kim, S., Moon, G., Yi, M., Park, K., Kim, Y., and Jun, E., "Parametric study on the flight envelope of a radio-frequency ion thruster based atmosphere-breathing electric propulsion system," *Acta Astronautica*, Vol. 212, 2023, pp. 198–212.
- ⁶ Moon, G., Yi, M., and Jun, E., "Design and operational concept of a cryogenic active intake device for atmosphere-breathing electric propulsion," *Aerospace Science and Technology*, Vol. 151, 2024, pp. 109300.
- ⁷ Moon, G. and Jun, E., "Feasibility Analysis of a Cryogenic Active Intake Device for Atmosphere-Breathing Electric Propulsion," *33rd International Symposium on Rarefied Gas Dynamics (Göttingen, Germany)*, 2024.
- ⁸ Wu, J., Zheng, P., Zhang, Y., and Tang, H., "Recent development of intake devices for atmosphere-breathing electric propulsion system," *Progress in Aerospace Science*, Vol. 133, 2022, pp. 100848.
- ⁹ Shoda, K., Kano, N., Jotaki, Y., Ezaki, K., Itatani, K., Ozawa, T., Yamashita, Y., Nishiyama, K., Yokota, K., and Tagawa, M., "Anisotropic molecular scattering at microstructured surface for rarefied gas compression inside air breathing ion engine," *CEAS Space Journal*, Vol. 15, 2023, pp. 403–411.
- ¹⁰ Nishiyama, K., "Air breathing ion engine concept," *54th International Astronautical Congress (IAC paper) (Bremen, Germany)*, 2003, pp. 2003–S.4.02.
- ¹¹ Jackson, S. W. and Marshall, R., "Conceptual design of an air-breathing electric thruster for CubeSat applications," *Journal of Spacecraft and Rockets*, Vol. 55, 2018, pp. 632–639.
- ¹² Romano, F., Espinosa-Orozco, J., Pfeiffer, M., Herdrich, G., Crisp, N. H., Roberts, P. C., Holmes, B. E., Edmondson, S., Haigh, S., Livadiotti, S., Macario-Rojas, A., Oiko, V. T., Sinpelru, L. A., Smith, K., Becedas, J., Sulliotti-Linner, V., Bisgaard, M., Christensen, S., Hanessian, V., Jensen, T. K., Nielsen, J., Chan, Y. A., Fasoulas, S., Traub, C., García-Almíñana, D., Rodríguez-Donaire, S., Sureda, M., Kataria, D., Belkouchi, B., Conte, A., Seminari, S., and Villain, R., "Intake design for an Atmosphere-Breathing Electric Propulsion System (ABEP)," *Acta Astronautica*, Vol. 187, 2021, pp. 225–235.
- ¹³ Zheng, P., Wu, J., Wu, B., and Zhang, Y., "Design and numerical investigation on the intake of atmosphere-breathing electric propulsion," *Acta Astronautica*, Vol. 188, 2021, pp. 215–228.
- ¹⁴ Zheng, P., Wu, J., Zhang, Y., and Zhao, Y., "Design and Optimization of vacuum Intake for Atmosphere-Breathing electric propulsion (ABEP) system," *Vacuum*, Vol. 195, 2022, pp. 110652.
- ¹⁵ Rapisarda, C., Roberts, P. C., and Smith, K. L., "Design and optimisation of a passive Atmosphere-Breathing Electric Propulsion (ABEP) intake," *Acta Astronautica*, Vol. 202, 2023, pp. 77–93.
- ¹⁶ Levchenko, I., Xu, S., Mazouffre, S., Lev, D., Pedrini, D., Goebel, D., Garrigues, L., Taccogna, F., and Bazaka, K., "Perspectives, frontiers, and new horizons for plasma-based space electric propulsion," *Physics of Plasmas*, Vol. 27, 2020, pp. 020601.
- ¹⁷ Jin, X., Miao, W., Cheng, X., Wang, Q., and Wang, B., "Monte Carlo Simulation of Inlet Flows in Atmosphere-Breathing Electric Propulsion," *AIAA Journal*, Vol. 62, No. 2, 2024, pp. 518–529.
- ¹⁸ Fontanarosa, D., Toscano, A. M., Ficarella, A., and Giorgi, M. G. D., "Direct simulation Monte Carlo-driven optimization of vacuum intakes for air-breathing electric thrusters in very low earth orbits," *Physics of Fluids*, Vol. 36, 2024, pp. 107135.
- ¹⁹ Yakunchikov, A., Kosyanchuk, V., Filatyev, A., and Golikov, A., "Simulation of rarefied gas flow inside the satellite air intake in ultra-low Earth orbit," *Acta Astronautica*, Vol. 226, 2025, pp. 102–112.



²⁰ Li, Y., Chen, X., Li, D., Xiao, Y., Dai, P., and Gong, C., “Design and analysis of vacuum air-intake device used in air-breathing electric propulsion,” *Vacuum*, Vol. 120, 2015, pp. 89–95.

²¹ Moon, G., Ko, Y., Yi, M., and Jun, E., “Operational Feasibility Analysis of a Cryogenic Active Intake Device for Atmosphere-Breathing Electric Propulsion,” *arXiv preprint arXiv:2503.02021*, 2025.

²² Yi, M., Choi, H., Park, K., Moon, G., Park, I., Huh, S., and Jun, E., “Characterization analysis of intake device for Atmosphere-Breathing Electric propulsion,” *AIAA SciTech Forum (AIAA paper 2025-0510) (Orlando, FL)*, 2025.

²³ Moon, G. and Jun, E., “Performance Study of Intake Device for Atmosphere-Breathing Electric Propulsion,” *AIP Conference Proceedings (32nd International Symposium on Rarefied Gas Dynamics)*, Vol. 2996, 2024, pp. 150005.

²⁴ Andreussi, T., Ferrato, E., and Giannetti, V., “A review of air - breathing electric propulsion : from mission studies to technology verification,” *Journal of Electric Propulsion*, Vol. 1, 2022, pp. 31.

²⁵ Hruby, V., Hohman, K., and Szabo, J., “Air Breathing Hall Effect Thruster Design Studies and Experiments,” *37th International Electric Propulsion Conference (IEPC paper 2022-446)*, 2022.

²⁶ Andreussi, T., Ferrato, E., Paissoni, C. A., Kitaeva, A., Giannetti, V., Piragino, A., Schäff, S., Katsonis, K., Berenguer, C., Kovacova, Z., Neubauer, E., Tisaev, M., Karadag, B., Lucca Fabris, A., Smirnova, M., Mingo, A., Le Quang, D., Alsalihi, Z., Bariselli, F., Parodi, P., Jorge, P., and Magin, T. E., “The AETHER project: development of air-breathing electric propulsion for VLEO missions,” *CEAS Space Journal*, 2022.

²⁷ Prochnow, F., Peter, C., Wulfkühler, J.-P., Drobny, C., Tajmar, M., Cook, J., Sparkes, M., O’neill, W., and Lockwood, N., “Development of a Novel Passively Ionizing Air-Breathing Electric Propulsion Concept for Low Earth Orbits,” *37th International Electric Propulsion Conference (IEPC paper 2022-420)*, 2022.

²⁸ Lieberman, M. A. and Lichtenberg, A. J., *Principles of Plasma Discharges and Materials Processing*, John Wiley & Sons, 2005.

²⁹ Choi, M., Yim, J. T., Williams, G. J., Herman, D. A., and Gilland, J. H., “Hybrid-PIC Simulation of Backspattered Carbon Transport in the Near-Field Plume of a Hall Thruster,” *35th International Electric Propulsion Conference (IEPC paper 2017-537)*, 2017.

³⁰ Tagawa, M., Yokota, K., Nishiyama, K., Kuninaka, H., Yoshizawa, Y., Yamamoto, D., and Tsuboi, T., “Experimental study of air breathing ion engine using laser detonation beam source,” *J. Propuls. Power*, Vol. 29, 2013, pp. 501–506.

³¹ Cushen, A. T., Oiko, V. T. A., Smith, K. L., Crisp, N. H., Roberts, P. C. E., Romano, F., Papavramidis, K., and Herdrich, G., “Performance Test Methodology for Atmosphere-Breathing Electric Propulsion Intakes in an Atomic Oxygen Facility,” *arxiv.org/abs/2406.06299*, 2024.

³² Parodi, P., Le Quang, D., Lapenta, G., and Magin, T., “Particle-in-Cell simulation of the VKI DRAG-ON facility,” *AIAA SciTech Forum (AIAA 2024-2710) (Orlando, FL)*, 2024.

³³ Bird, G. A., *Molecular Gas Dynamics and the Direct Simulation of Gas Flows*, Clarendon Press, 1994.

³⁴ Moon, G., Choe, W., and Jun, E., “Plasma plume simulation of an atomic oxygen-fed ion thruster in very-low-earth-orbit,” *Plasma Sources Science and Technology*, Vol. 32, No. 12, 2023, pp. 125012.

³⁵ Boyd, I. D. and Dressler, R. A., “Far field modeling of the plasma plume of a Hall thruster,” *Journal of Applied Physics*, Vol. 92, No. 4, 2002, pp. 1764–1774.

³⁶ Tumuklu, O. and Levin, D. A., “Particle simulations of the effects of atomic oxygen on ion thruster plumes,” *Journal of Spacecraft and Rockets*, Vol. 55, No. 5, 2018, pp. 1154–1165.

³⁷ Miller, J. S., Pullins, S. H., Levandier, D. J., Chiu, Y. H., and Dressler, R. A., “Xenon charge exchange cross sections for electrostatic thruster models,” *Journal of Applied Physics*, Vol. 91, No. 3, 2002, pp. 984–991.



³⁸ Andrews, S. and Berthoud, L., "Characterising satellite aerodynamics in Very Low Earth Orbit inclusive of ion thruster plume-thermosphere/ionosphere interactions," *Acta Astronautica*, Vol. 170, 2020, pp. 386–396.

³⁹ Stephani, K. A. and Boyd, I. D., "Detailed modeling and analysis of spacecraft plume/ionosphere interactions in low Earth orbit," *Journal of Geophysical Research: Space Physics*, Vol. 119, No. 3, 2014, pp. 2101–2116.

⁴⁰ Rapp, D. and Francis, W. E., "Charge exchange between gaseous ions and atoms," *The Journal of Chemical Physics*, Vol. 37, No. 11, 1962, pp. 2631–2645.

⁴¹ Yim, J. T., "A Survey of Xenon Ion Sputter Yield Data and Fits Relevant to Electric Propulsion Spacecraft Integration," *35th International Electric Propulsion Conference (IEPC paper 2017-060)*, 2017.

⁴² Eckstein, W. and Preuss, R., "New fit formulae for the sputtering yield," *Journal of Nuclear Materials*, Vol. 320, 2003, pp. 209–213.

⁴³ Wei, Q., Li, K. D., Lian, J., and Wang, L., "Angular dependence of sputtering yield of amorphous and polycrystalline materials," *Journal of Physics D: Applied Physics*, Vol. 41, 2008, pp. 172002.

⁴⁴ Sigmund, P., *Sputtering by ion bombardment theoretical concepts*, Springer Berlin Heidelberg, Berlin, Heidelberg, 1981, pp. 9–71.

⁴⁵ Tekinalp, A. and Levin, D. A., "3D detailed far field plume modeling of SPT-100," *AIAA Propulsion and Energy Forum and Exposition (AIAA paper 2019-3989)*, 2019.

⁴⁶ Merino, M., Cichocki, F., and Ahedo, E., "A collisionless plasma thruster plume expansion model," *Plasma Sources Science and Technology*, Vol. 24, No. 3, 2015.

⁴⁷ Moon, G. and Jun, E., "Plume simulation of atmosphere-breathing electric propulsion system," *AIP Conference Proceedings (32nd International Symposium on Rarefied Gas Dynamics)*, Vol. 2996, 2024, pp. 150006.

⁴⁸ Merino, M., Fajardo, P., Giono, G., Ivchenko, N., Gudmundsson, J. T., Mazouffre, S., Loubère, D., and Dannenmayer, K., "Collisionless electron cooling in a plasma thruster plume: Experimental validation of a kinetic model," *Plasma Sources Science and Technology*, Vol. 29, 2020, pp. 035029.

⁴⁹ Plimpton, S. J., Moore, S. G., Borner, A., Stagg, A. K., Koehler, T. P., Torczynski, J. R., and Gallis, M. A., "Direct simulation Monte Carlo on petaflop supercomputers and beyond," *Physics of Fluids*, Vol. 31, 2019, pp. 086101.

⁵⁰ Huh, S., Moon, G., and Jun, E., "Drag analysis incorporating atomic oxygen adsorption in Very-Low-Earth-Orbit," *Aerospace Science and Technology*, Vol. 158, 2025, pp. 109900.

⁵¹ Huh, S., Moon, G., and Jun, E., "Numerical Analysis of Atomic Oxygen Adsorption Using Direct Simulation Monte Carlo in Very-Low-Earth-Orbit," *33rd International Symposium on Rarefied Gas Dynamics (Göttingen, Germany)*, 2024.

⁵² Murray, V. J., Pilinski, M. D., Smoll, E. J., Qian, M., Minton, T. K., Madzunkov, S. M., and Darrach, M. R., "Gas-Surface Scattering Dynamics Applied to Concentration of Gases for Mass Spectrometry in Tenuous Atmospheres," *Journal of Physical Chemistry C*, Vol. 121, 2017, pp. 7903–7922.

⁵³ Xu, C., Murray, V. J., Pilinski, M. D., Schwartentruber, T. E., Poovathingal, S. J., and Minton, T. K., "Gas concentration in rarefied flows: Experiments and modeling," *Aerospace Science and Technology*, Vol. 142, 2023, pp. 108568.

⁵⁴ Park, W. and Jun, E., "Effects of Surface Corrugation on Gas-Surface Scattering and Macroscopic Flows," *arXiv preprint arXiv:2504.04755*, 2025.

